Large eddy simulation of heat transfer around a square cylinder using unstructured grids

M. Boileau, F. Duchaine, J.-C. Jouhaud, Y. Sommerer

Large eddy simulation of heat transfer around a square cylinder using unstructured grids

M. Boileau[1], F. Duchaine[2] and J.-C. Jouhaud[2]
CERFACS, Toulouse, France, 31057

Y. Sommerer[3]
AIRBUS (EADS group), Toulouse, France, 31060

This paper presents a method of large eddy simulation on unstructured grids designed to predict the wall heat transfer in typical aeronautical applications featuring turbulent flows and complex geometries. Two types of wall treatment are considered: a wall-function model using a full tetrahedral grid and a wall-resolved method computed on a hybrid tetrahedral-prismatic grid. These two approaches are tested against the square cylinder case at moderate Reynolds number ($Re = 22\,050$) where many reference data are available for flow dynamics and heat transfer. Both predict accurately the unsteady flow around the cylinder and in its near-wake but only the wall-resolved approach reproduces the Nusselt number global value and its spatial distribution around the cylinder wall. This latter method is used to investigate the coupling between periodic vortex shedding and wall heat transfer using a phase-averaged analysis.

Nomenclature

C_D = drag coefficient

C_f = algebraic friction coefficient

C_p = pressure coefficient

---

[1] Postdoctoral researcher at CERFACS, now CNRS research engineer at EM2C laboratory, CNRS UPR288, Ecole Centrale Paris, 92295 Châtenay-Malabry Cedex, France
[2] Senior researcher, CERFACS, 42 avenue Gaspard Coriolis, 31057 Toulouse Cedex 01, France
[3] Research engineer, EEI5 Engine Integration, AIRBUS France, M0112/5, 316 Route de Bayonne, 31060 Toulouse Cedex 09, France

D = cylinder diameter, m

E = channel span, m

h = channel height, m

l_r = length of recirculation zone

M = Mach number

Nu = local Nusselt number

Nu_g = global Nusselt number

Pr = Prandtl number

Re = Reynolds number

q = heat flux, $\mathrm{W.m^{-1}}$

Sc = Schmidt number

Sh = Sherwood number

St = Strouhal number

T = temperature, K

t_c = convective time

t_{av} = average time

t_{sh} = vortex shedding time

t^+ = non dimensional time

U = velocity, $\mathrm{m.s^{-1}}$

u = non dimensional axial velocity

v = non dimensional transverse velocity

y^+ = wall Reynolds number

Δx = size of triangle faces

Δh = height of prism cells

λ = thermal conductivity, $\mathrm{W.m^{-1}.K^{-1}}$

μ = dynamic viscosity, $\mathrm{kg.m^{-1}.s^{-1}}$

ν = cinematic viscosity, $\mathrm{m^2.s^{-1}}$

ϕ = phase of vortex shedding, $^\circ$

ρ = density, $\mathrm{kg.m^{-3}}$

$\overline{}$ = time average (except in section II A: LES filtering)

$\tilde{}$ = Favre filtering

$\langle\ \rangle$ = phase average

Subscripts

sgs = subgrid scale quantity

$wall$ = wall quantity

∞ = freestream condition

f = film condition

I. Introduction

Turbulent heat transfer in industrial configurations usually occurs in complex geometries where flow separation and vortex shedding take place. For example, in a turbo-engine nacelle compartment, the thermal integration of some dissipative equipment (valves, pumps, generator, etc.) requires to use models to assess convective, conductive and radiative heat transfer. Those equipments represent bluff-bodies that sometimes must be air-cooled to be protected from internal heat loads and/or from the strong heat flux coming from the engine case. An accurate prediction of the local convective heat transfer is crucial to design and optimize the cooling system with the double objective of improving the equipment reliability and preserving the aircraft performance. Such prediction requires a computational method that captures accurately the aerodynamic features of the flow: back flows, vortex shedding, wakes, cooling jets, interactions, etc. Classical industrial CFD tools using a statistical (RANS) approach fail to reproduce this type of flows where the unsteady component may be superior than the main flow due to large eddy turbulent scales and low bulk velocities. However, the large eddy simulation (LES) approach is a promising method because of its ability to solve explicitly these large scale motions. The aim of this work is to develop a LES methodology that can be applied to convective heat transfer problems in industrial configurations. This methodology must guaranty a given precision at a controlled CPU cost.

For the targeted problems, a special attention must be paid to the near-wall modeling. Using enough grid resolution and a proper subgrid model, LES can behave like direct numerical simulation (DNS) when approaching the wall boundary. Thus, a wall-resolved LES should accurately predict the wall heat flux in any flow configuration without any specific wall treatment. However, its computational cost may be very expensive for high Reynolds flows because solving the boundary

layer leads to large computational grids and small time steps. The least expensive way to account for near-wall effects in LES is to model the boundary layer using a wall-function. Such an approach has been implemented and tested in a complex geometry LES calculation by Schmitt *et al.* [1]. Nevertheless, in a typical industrial geometry where flow separation occurs, the validity of this wall-function is questionable. In the present paper, both the wall-resolved and wall-function approaches are evaluated.

For most cases of industrial internal flows, the physical domain cannot be meshed using a structured grid and requires an unstructured grid composed of tetrahedral elements. So, the unstructured grid technique is retained here. This choice have a strong impact on the numerical approach used to solve the flow equations. For the same spatial resolution, an unstructured grid calculation is usually more expensive and less accurate than a calculation on a structured grid. Consequently, conclusions that are drawn on a LES test case using a structured grid may not be relevant for an unstructured grid approach. Indeed, the choice of the best LES model, the grid refinement criterion, the type of wall modeling, etc., depend on the type of grid.

Before being applied to real cases and complex geometries, the present numerical tool must be validated for heat transfer prediction in a simple well-documented configuration. The flow past a square cylinder was found to be a good candidate for the validation of turbulent heat transfer by forced convection. First, extensive unsteady experimental results are available as reference data for the flow dynamics. Second, this configuration has been used as benchmark case for many isothermal LES studies in the past. Third, two different experimental studies provide data for the wall heat flux distribution around the cylinder. Finally, the square cylinder case is typical of the bluff-body flows encountered in practical configurations (thermal cooling for aeronautics or electronic devices, for example): flow impingement on the front face and flow separation on the side and rear faces with alternate vortex shedding and transient reattachment.

On the one hand, Bosch and Rodi [2, 3] have shown that some main dynamics quantities can be predicted in the square cylinder case using unsteady RANS but they found that such an approach misses the details of the complex 3D flow, specially the 3D turbulent motion near the wall which is involved in the heat transfer. On the other hand, several isothermal LES studies on structured

grids have been performed based on this flow configuration [4–8]. From the authors knowledge, the work of Camarri *et al.* [9] is the only LES of the square cylinder case performed on an unstructured grid. All these numerical studies compare the LES results with the experimental data of Lyn and Rodi [10] for the shear layer region and of Lyn *et al.* [11] for the wake flows (some of them also compare with former experimental data of Bearman and Obasaju [12] and Durao *et al.* [13]). References [10] and [11] provide phase-averaged experimental analyzes in order to investigate the vortex shedding phenomena. Two LES studies give some comparisons with these phase-averaged data [4, 7]. Concerning heat transfer, only experimental data are available. Both Igarashi [14] and Yoo *et al.* [15] provide the mean profiles of Nusselt number around the cylinder for various Reynolds numbers. Based on his own results, Igarashi [14] also proposes an empirical correlation for the global Nusselt number as a function of the Reynolds number. The present LES consider the flow and heat transfer past an isothermal square cylinder at Reynolds $Re = 22\,050$, a value that corresponds to the reference experiments [10] and [11] for flow dynamics and that belongs to a range where the mentioned heat transfer data are available.

The originality of the present work is to evaluate the prediction of both the flow dynamics and heat transfer from the wall in a well-documented configuration with LES methods using unstructured grids. Two different approaches are used for the near-wall treatment: an algebraic wall-function model on a full tetrahedra grid and a wall-resolved technique using a hybrid tetrahedra/prisms grid. Because wall-resolved computations are expensive in terms of CPU time, the numerical tools is designed to run on massively parallel architectures. Dealing with practical cases, the real geometries make the flow topology much more complex than for a single obstacle. For instance, the wake of an upstream obstacle can strongly influence the flow and heat transfer around a downstream body. Thus, some of the present study focuses on the capability of the method to predict the near wake flow dynamics.

The paper is organized as follow. In section II, the LES solver and the near-wall modeling are presented. The flow configuration is introduced in section III giving a description of the physical conditions, the reference experimental data, the meshing strategy and the averaging procedure. In section IV, results are compared with experimental and LES data in order to validate the flow dy-

namics and thermal predictions. The mechanism of heat transfer from the wall is finally investigated using an unsteady analysis of the LES results.

II. LES of anisothermal flows

A. LES equations

A summary of the compressible LES equations solved by the code is given below (see Moureau *et al.* [16] for detailed description).

$$\frac{\partial \overline{\mathbf{w}}}{\partial t} + \nabla \cdot \overline{\mathbf{F}} = 0 \tag{1}$$

where $\overline{\mathbf{w}}$ is the vector of conservative variables ($\overline{\ }$ denotes the LES filtering) and $\overline{\mathbf{F}}$ is the flux tensor composed of viscous, inviscid and subgrid scale component. $\overline{\mathbf{w}}$ is given by:

$$\overline{\mathbf{w}} = \left(\overline{\rho}, \overline{\rho}\tilde{u}, \overline{\rho}\tilde{v}, \overline{\rho}\tilde{w}, \overline{\rho}\tilde{E}\right) \tag{2}$$

In Eq. (2), $\overline{\rho}$ is the density, $(\tilde{u}, \tilde{v}, \tilde{w})$ are the velocity components ($\tilde{\ }$ denotes the Favre averaging), $\tilde{E} = \tilde{e}_s + 1/2\tilde{u}_i\tilde{u}_i$ is the total energy, where $\tilde{e}_s$ is the sensible energy related to the temperature $\tilde{T}$ through the constant volume heat capacity C_v ($de_s = C_v dT$). $\overline{\mathbf{F}}$ contains in particular the resolved conductive heat flux $\overline{\mathbf{q}}$ which is estimated by the Fourier's law:

$$\overline{q}_i = -\overline{\lambda}\frac{\partial \tilde{T}}{\partial x_i} \qquad \text{where:} \quad \overline{\lambda} = \frac{\overline{\mu} C_p(\tilde{T})}{Pr} \tag{3}$$

In Eq. (3), $\overline{\lambda}$ is the thermal conductivity, C_p is the constant pressure heat capacity, Pr is the Prandtl number ($Pr = 0.71$ for air) and $\overline{\mu}$ is the dynamic viscosity given by the Sutherland's law. Assuming an eddy diffusivity and using the Reynolds analogy, the subgrid conductive flux $\overline{\mathbf{q}}^{sgs}$ is given by:

$$\overline{\mathbf{q}}_i^{sgs} = -\overline{\lambda}_{sgs}\frac{\partial \tilde{T}}{\partial x_i} \qquad \text{where:} \quad \overline{\lambda}_{sgs} = \frac{\overline{\mu}_{sgs} C_p(\tilde{T})}{Pr_{sgs}} \tag{4}$$

where Pr_{sgs} is the subgrid Prandtl number ($Pr_{sgs} = 0.9$) and $\overline{\mu}_{sgs}$ is the subgrid viscosity provided by the subgrid model (see section II C).

In order to simplify the notations and to avoid confusion with the temporal average, LES quantities are noted without any $\overline{\ }$ in the following.

B. LES solver

The present approach uses the in-house AVBP code to solve the fully compressible LES system described by Eq. (1) (see Ref. [16]). The cell-vertex unstructured formulation makes it easily applicable to complex geometries [17]. Centered spatial schemes and explicit time-advancement are used to control numerical dissipation. For the present case, two numerical schemes have been employed: a second order finite-volume Lax-Wendroff scheme and a third order finite-element TTGC scheme [18]. The explicit time step Δt is imposed by the CFL condition:

$$CFL = \frac{(U+c)\Delta t}{\Delta x} \approx 0.7 \tag{5}$$

where Δx is the size of the grid cell while U and c are the flow and sound local velocities respectively. The calculation time step is taken as the minimum of Δt in Eq. (5) over the whole domain.

To model the subgrid viscosity $\overline{\mu}_{sgs}$, two subgrid scale models have been applied according to the treatment applied at the wall (see later): the classic Smagorinsky model and the WALE model [19]. Finally, characteristic boundary conditions NSCBC [16, 20] are used for the inlet and the outlet.

Using the MPI library, the LES code offers a very good efficiency on a high number of processors and can run on today's largest parallel computors [21]. The present calculation has been run on a Cray XD1 and on an IBM BladeCenter using 16 to 64 cores. Some computational resources provided by an IBM BlueGene/L on 512 cores have also been used.

C. Near-wall modelling

Different strategies to model the turbulent boundary layer in the context of LES are reviewed in Piomelli and Balaras [22]. In the present case, two approaches are compared: a wall-resolved LES (called *LES-WR*) and a LES using wall-functions (called *LES-WF*). In the wall-resolved case, the subgrid scale effects are modelled by the WALE model [19] which is notably able to recover the proper y^3 damping scaling for eddy viscosity at the wall without requiring any damping function nor dynamic procedure. To provide the right viscous stress and heat flux at the wall, the grid cells adjacent to the wall must be inside the viscous sublayer. This condition requires a high density of very small grid cells close to the wall, i.e. large grids and small time steps (see Eq. (5)) which leads to expensive CPU costs. However, this approach is expected to be the most accurate since it solves

explicitely the flow and the heat transfer inside the turbulent boundary layer.

A less CPU-consuming approach is to model momentum and heat transfer in the boundary layer using wall-functions. Compared to more sophisticated methods like zonal approaches or hybrid LES/RANS approaches, algebraic wall-functions are easier to implement in a unstructured code. Details on these wall-functions and how they are implemented in the present LES code are given in Schmitt *et al.* [1] and only essential informations are given here. The principle of the wall-function is to model the wall shear stress τ_{wall} and the wall heat flux q_{wall} given the following quantities:

- the velocity u_2 and the temperature T_2 at the first interior grid point,
- the cell height y_{wall} normal to the wall,
- the viscosity ν_{wall}, density ρ_{wall}, heat capacity $C_{p,wall}$ and temperature T_{wall} at the wall-face.

The non-dimensional variables wall-distance y^+ and velocity u^+ of the first interior grid point are defined by:

$$y^+ = \frac{y_{wall} u_\tau}{\nu_{wall}} \quad \text{and} \quad u^+ = \frac{u_2}{u_\tau} \tag{6}$$

where $u_\tau = (\tau_{wall}/\rho_{wall})^{1/2}$ is the friction velocity. Based on experimental results in channel flows, the following equations give u^+ as a function of y^+:

$$u^+ = y^+ \quad \text{if} \quad y^+ \leq 11.445 \tag{7}$$

$$u^+ = \frac{1}{\kappa} \ln y^+ + C \quad \text{if} \quad y^+ > 11.445 \tag{8}$$

where $\kappa = 0.41$ is the von Karman constant and $C = 5.5$ is an integration constant. Then, the non-dimensional temperature is defined by:

$$T^+ = \frac{\rho_{wall} C_{p,wall} u_\tau \left(T_{wall} - T_2\right)}{q_{wall}} \tag{9}$$

Using the Reynolds analogy, the wall heat flux is given by the following model:

$$T^+ = Pr y^+ \quad \text{if} \quad y^+ \leq 11.445 \tag{10}$$

$$u^+ = \frac{1}{\kappa} \ln y^+ + C_T \quad \text{if} \quad y^+ > 11.445 \tag{11}$$

where $C_T = 3.9$ is an integration constant.

The wall heat flux is used to compute the local Nusselt number:

$$Nu = \frac{q_{wall} D}{\lambda_{wall}(T_{wall} - T_\infty)} \tag{12}$$

where:

- q_{wall} is explicitely given by Eq. (9) in the *WF* approach,
- $q_{wall} = q_n + q_n^{sgs}$ in the *WR* approach, n being the wall normal direction and q_n and q_n^{sgs} the respective resolved and subgrid normal heat flux given by Eq. (3) and (4). In practice, q_n^{sgs} is close to zero since the subgrid flux predicted by the WALE model tends to zero at the wall when the boundary is fully resolved. In the present case, q_n^{sgs} contributes less than 0.3% of the mean q_{wall} of the cylinder.

III. Configuration

A. Geometry and physical conditions

The computational domain is described by Fig. 1. The vertical dimension was fixed in order to match a blockage ratio of $h/D = 14$. Inlet and outlet boundary conditions were placed sufficiently far from the cylinder to prevent boundaries from influencing the flow around it and in its near-wake. To mimic the large spanwise extent of the experiment of Lyn *et al.* [10] ($E/D = 9.75$), a periodic condition was applied to the lateral sides and the spanwise extent was set to $E/D = 4$, a value commonly accepted in previous studies and that verifies convergence tests performed here on global quantities (drag coefficient and Nusselt number). In Lyn *et al.*'s experiment, the fluid is water and the upstream Mach number M_∞ is very low ($M_\infty = 3.57 \times 10^{-4}$). Computing such Mach number flow with the present compressible approach would be meaningless. Indeed, in the case of low Mach number flow ($U \ll c$), the number of temporal iterations N_{ite} needed to simulate one flow-through time $t_c = (D/U_\infty)$ in an explicit compressible solver can be expressed by:

$$N_{ite} \approx \frac{1}{M\,CFL} \frac{D}{\Delta x} \tag{13}$$

where D is a characteristic length scale. Equation (13) shows that $N_{ite} \to \infty$ when $M \to 0$. In the present case, water is replaced by air and the upstream Mach number is set to $M_\infty = 0.108$

so that the computational cost remains reasonable and the flow still respects the incompressible assumption (the maximum local instantaneous Mach number is less than 0.2). Giving that Mach number scaling, using a compressible formulation for an incompressible anisothermal flow has two advantages: on one hand, it captures intrinsically the variation of density with temperature, on the other hand, the problem can be solved by an explicit numerical scheme which is well adapted to massively parallel computing. Freestream velocity and temperature are imposed at the inlet while pressure is imposed at the outlet (see Fig. 1) through non reflecting NSBC type boundary conditions. The blockage effect is applied using slip walls at the top and bottom boundaries.

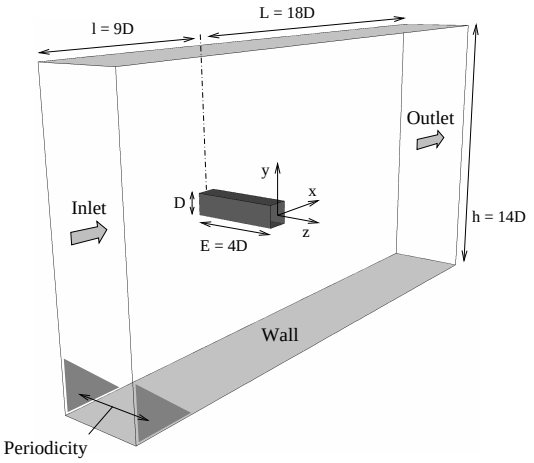

Fig. 1 Global view of the computational domain and boundary conditions.

Heat transfer from the square cylinder to the air flow is applied through an isothermal wall condition with a uniform temperature $T_{wall} = 330$ K while the upstream flow is at $T_\infty = 300$ K. Since this temperature jump is quite small, the fluid temperature is expected to behave like a passive scalar having a negligible effect on the flow hydrodynamics. Note that for industrial applications where this passive scalar assumption may be not verified, the present method is still valid since the compressible formulation fully accounts for the variation of density with temperature. In the present case, the variation of the temperature in the boundary layer induces a variation of the fluid transport properties. So, the Reynolds number $Re = U_\infty D/\nu$ has been calculated from the cinematic viscosity $\nu = \mu/\rho$ taken at the film temperature $T_f = 1/2\,(T_\infty + T_{wall})$. Computing ν from T_∞ or T_{wall} instead of T_f would result in 10% error on the Reynolds number. The physical

parameters of the simulated cases are presented in Table 1. In the following, lengths are normalized by D, velocities by U_∞ and times by $t_c = D/U_\infty$.

Table 1 Physical parameters of the LES cases.

Upstream velocity:	$U_\infty = 37.7$ m.s^{-1}
Upstream temperature :	$T_\infty = 300$ K
Upstream Mach number:	$M_\infty = 0.108$
Cylinder diameter:	$D = 1$ cm
Cylinder temperature:	$T_{wall} = 330$ K
Film temperature:	$T_f = 315$ K
Reynolds number:	$Re = 22\,050$
Outlet pressure:	$p_{out} = 101\,325$ Pa

B. Reference experimental and numerical data

As flow dynamics is concerned, various experimental and LES results are available in the literature. Using laser-Doppler velocimetry (LDV), Lyn and Rodi [10] have investigated the velocity field in the flapping shear layer region occurring on the close top and bottom faces of the cylinder. They provide statistics from time-averaged as well as phase-averaged data which can be used to evaluate how the LES predicts the periodic flow due to the alternate vortex shedding. In a following paper, Lyn *et al.* [11] provide the same type of data for the near-wake region where the well-known von Kármán-Bénart instability develops. These data are used here to validate the prediction of this instability by the LES. They are completed with some LDV measurements at $Re = 14\,000$ by Durao *et al.* [13]. Other velocity data obtained using phase-Doppler anemometry by Fohanno & Martinuzzi [23] are also included as a third experimental reference. Dealing with mean and fluctuating pressure coefficient around the cylinder wall, the present LES results are compared with experimental profiles of Bearman and Obasaju [12] at $Re = 20\,000$ and of Igarashi [24] at $Re = 37\,000$. In terms of LES results, the data of Hangan and Kim [25] are utilized for comparison of time-averaged velocity profiles in the shear layer and near-wake regions. For phase-average profiles in the near wake, the LES by Liou *et al.* [7] and Rodi *et al.* [4] (case *KAWAMU* which is the best reproduction

of the experimental results) are referred. For global quantities such as drag coefficient, Strouhal number and recirculation length, the previously mentioned experimental and numerical results are used in addition with those of Oudheusden *et al.* [26], Fureby *et al.* [6], Barone *et al.* [8] and Camarri *et al.* [9] (see Table 3).

Dealing with heat transfer, Igarashi's correlation [14] provides a reference for the global Nusselt number. According to Sparrow *et al.* [27], it is "the best current representation of the average Nusselt number results for a square cylinder in cross-flow". This correlation is given below with the Sieder-Tate correction to account for the variation of viscosity:

$$\overline{Nu}_g = 0.14 \left(\frac{\mu_\infty}{\mu_{wall}} \right)^{0.14} Re^{0.66} \tag{14}$$

which is valid for $5\,000 \leqslant Re \leqslant 60\,000$. Igarashi [14] also measured the profiles of local Nusselt number around the cylinder at given Reynolds numbers using thermocouples. However, none of these Reynolds values corresponds to the present one ($Re_{LES} = 22\,050$) which has been fixed in order to match the Lyn and Rodi experiment. Therefore, Igarashi's correlation has been used to scale the two Igarashi's Nusselt profiles corresponding to the closest Reynolds values ($Re_{exp} = 18\,500$ and $29\,600$):

$$\overline{Nu}_s = \overline{Nu}_{exp} \left(\frac{\mu_\infty}{\mu_{wall}} \right)^{0.14} \left(\frac{Re_{LES}}{Re_{exp}} \right)^{0.66} \tag{15}$$

As proved later in the article (Fig. 19), the scaled experimental profiles match closely which justifies the use of Eq. (15). Using the analogy between heat and mass transfer, the Nusselt profiles can be deduced from the Sherwood (Sh) profiles measured by Yoo *et al.* [15] with the naphthalene sublimation technique. This analogy is expressed by the law: $Nu = Sh\,(Pr/Sc)^{1/3}$, where Pr is the Prandtl number of air ($Pr = 0.71$) and Sc is the Schmidt number of Naphatalene ($Sc = 2.53$, obtained by the correlation of Cho *et al* [28] taken at the temperature of Yoo *et al.*'s experiment $T = 303\,\mathrm{K}$).

C. Meshing strategies and numerical parameters

Tetrahedral elements are suitable for complex geometries because they have the capability to fill a given volume of arbitrary shape. Moreover, in large eddy simulation, tetrahedral grids makes

it possible to use coarse cells where only the largest scales are of interest while refining the regions of high solution gradients and turbulence production. In order to limit the spatial commutation errors that arise inevitably when using an implicit filtering method, the grid is stretched at a moderate rate in the region of interest. To mesh the near-wall region, two strategies have been tested according to the near-wall modelling approach:

A full tetrahedral grid for the wall-function case (case *LES-WF*): This meshing technique provides the easiest and fastest way to generate a grid in a complex geometry. Since tetrahedral elements are not adapted to solve the wall boundary layer, this meshing strategy is used along with the wall-function approach (see section II C). As shown by Fig. 2, the grid is coarse far from the cylinder ($\Delta x = 0.5$), moderately refined in the near-wake region ($\Delta x = 0.1$) and strongly refined close to the cylinder ($\Delta x = 0.04$, see Fig. 3, case *LES-WF*). This refinement is expected to be sufficient to capture accurately the turbulent flow generated by the Kelvin-Helmoltz instability in the detached upper and lower shear-layers and by the von Kármán-Bénart instability in the cylinder wake. On the other hand, the size of the cells adjacent to the cylinder wall is supposed to be large enough to use the wall-function approach in the logarithmic region (Eq. (8)). Figure 5 shows the value of the Reynolds number y^+ of the first interior grid point around the cylinder (see section III D for the description of the averaging procedure used to obtain y^+). Most of y^+ values are in the range $20 - 30$ which is a little below the condition $y^+ > 30$ for the logarithmic law to be fully valid. However, the deviation of the u^+ and T^+ universal profiles from the log law is lower than 10% for $y^+ = 20$.

A hybrid tetrahedral-prismatic grid (case *LES-WR*): When the boundary layer is explicetely solved, using prismatic layers close to wall surfaces is more efficient than tetrahedra (see for example [29, 30]). First, quadrilateral faces normal to the wall provide good orthogonality and grid-clustering capabilities which are suitable to thin boundary layers, whereas the triangulation in the tangential direction keeps the flexibility in surface modeling. Second, for a same spatial resolution in the normal direction, the prisms layers use less elements and lead to a higher minimum cell volume than the full tetrahedral grid approach because prismatic elements can have a large aspect ratio. For the wall-resolved case (*LES-WR*), the near-wall

region has been meshed using five layers of prismatic elements (see Fig. 3) where the height of the layers, Δh, is smaller than the size of their triangle basis, Δx. To avoid numerical errors, the aspect ratio of the thinnest layer (inner layer adjacent to the wall) was limited to $\Delta x/\Delta h = 4$ far from the cylinder edges and $\Delta x/\Delta h = 3$ near the edges. Beyond these limits, the high velocity gradients (due to the shear layer) in region of strongly stretched cells may generate numerical instabilities under the form of unphysical cell-to-cell oscillations. The critical aspect ratio may depend on the flow configuration (i.e. the geometry of the bluff-body) as well as on the numerical method so the present values should not be considered as universal. The stretching ratio between the height of an inner layer to the adjacent outer layer was set to 1.13, leading to $1.83 < \Delta x/\Delta h < 2.45$ in the outer layer. The proper height of the inner prisms layer (Δh) was determined by a mesh convergence study based on the global Nusselt number $\overline{Nu}_g$ compared to the experimental correlation of Igarashi [14] (Eq. (14)). Figure 4 shows that $\Delta h \leq 0.002$ is required to match the empirical Nusselt number. The corresponding y^+ profile is plotted on Fig. 5. Most of the near-wall resolution is below $y^+ < 2$ but some regions close to the edges of the cylinder reach higher values. This point is discussed further in section IV B. Using this mesh constraint in the near-wall region and the same tetrahedral sizes as case *LES-WF* in other regions leads to a 3.3 million nodes grid (12.6 million cells). In comparison, a full tetrahedral grid having the same resolution would feature around 13 million nodes (60 million cells) with a smaller minimum cell volume requiring a time step four times shorter. Such a grid would cost 10 times more CPU time than the present hybrid grid. It is important to note that the benefit of using prismatic layers instead of tetrahedra depends strongly on the maximum acceptable $\Delta x/\Delta h$ ratio. Indeed, considering that the smallest height of the prismatic cells is imposed by the $y^+ \approx 1$ constraint, the number of prismatic cells scales like $(\Delta x/\Delta h)^{-2}$ while the time step — which is proportional to the minimum cell volume — scales like $(\Delta x/\Delta h)^2$. Therefore, assuming that the ratio between the number of prismatic cells N_P and the total number of cells N_{tot} varies little with $\Delta x/\Delta h$, we get the following law for the CPU cost dependence: $CPU_{cost} \propto \left(1 + N_P/N_{tot}\,(\Delta x/\Delta h)^{-2}\right)(\Delta x/\Delta h)^{-2}$. In the present case we have $N_P/N_{tot} \approx 1/4$ (see Table 2).

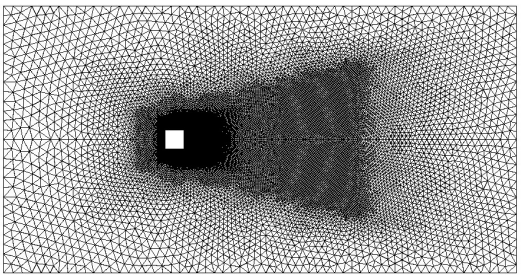

Fig. 2 Side view of the computational grid (valid for both cases).

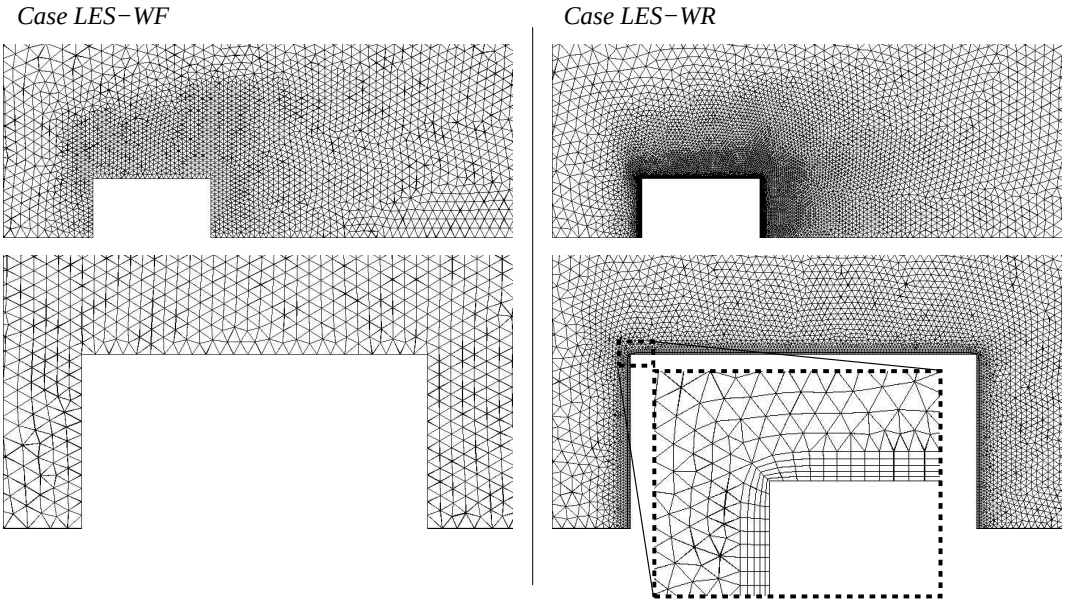

Fig. 3 Zooms on the side view of the top half of the two unstructured grids: full tetrahedral grid (case *LES-WF*) and hybrid prismatic/tetrahedral grid (case *LES-WR*). Bottom right image is a zoom on the five layers of prismatic elements.

Both grids were automatically created by the Centaur$^{\mathrm{TM}}$ grid generation software, from the mesh constraints described above. To ensure a perfect symmetry with respect to the plane xz and to reduce the grid generation time, a shorter domain comprising the upper top of the canal and one diameter spanwise extent ($E = D$) was first meshed. This pattern was then extended by mirror transformation and successive duplication/translation in the z (periodic) direction to produce the full computational domain ($E = 4D$) of Fig. 1. The characteristics of the grids obtained are compared in Table 2. Because the wall-resolved strategy leads to higher CPU costs, a second order Lax-Wendroff scheme was used for *LES-WR* whereas the *LES-WF* is computed with the 2.5 times more expensive

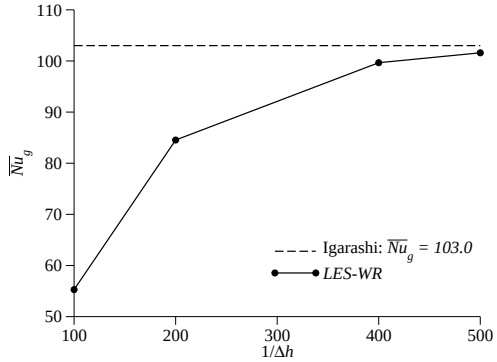

Fig. 4 Global Nussel number of the cylinder, $\overline{Nu}_g$, for the wall-resolved case *(LES-WR)* as a function of the mesh wall resolution $1/\Delta h$ compared to the experimental correlation of Igarashi [14] (Eq. (14))

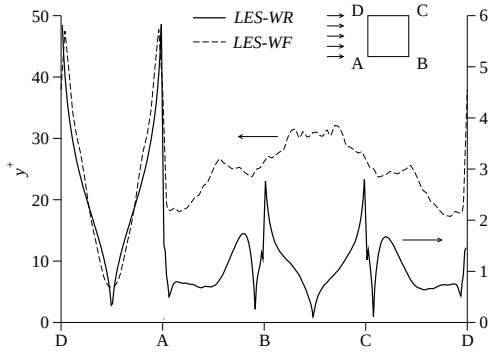

Fig. 5 Profiles of time-averaged wall Reynolds number of the first fluid node, y^+, around the cylinder.

third order TTGC scheme. One can note that, for a same physical time calculation, the wall-resolved LES costs 40 times more CPU time than the wall-function case because of a higher number of cells as well as a shorter time step. Using massively parallel computing, the shortest possible time of execution becomes more or less independent of the grid size (a larger grid can be calculated within the same execution time using more CPU cores since the speed-up on a massively parallel machine is mainly limited by the number of computational cells per parallel process). So, the minimum of execution time depends mostly on the number of iterations N_{ite} required to achieve one flow time t_c. According to Table 2, a minimum ratio of 5 between the execution time of cases *LES-WR* and

LES-WF could be obtained if the runs were not limited by the number of cores available.

Table 2 Characteristics of the two LES cases. N_{ite}/t_c **and** N_{ite}/t_{sh} **are the number of time iterations required to compute a flow time** (t_c) **and a vortex shedding time** (t_{sh}) **respectively.** t_{LES} **and** t_{av} **are the total physical time of the calculation and the time period used for averaging respectively.**

Cases	*LES-WF*	*LES-WR*
Type of element	Tetra	Tetra & prisms
Number of nodes	570 000	3 310 000
Number of cells	3 200 000	12 600 000
Number of prismatic cells	–	3 000 000
Smallest cell length Δx	0.04	0.006 – 0.008
Smallest cell height Δh	0.04	0.002
Wall treatment	wall-function	no-slip, isothermal
Numerical scheme	TTGC	Lax-Wendroff
N_{ite}/t_{sh}	8 500	43 800
t_{LES}/t_c (t_{av}/t_c)	192 (149)	148 (139)
t_{LES}/t_{sh} (t_{av}/t_{sh})	27 (20)	20 (18)
Total CPU hours	1 300	38 400

Both numerical scheme used here are centered schemes so they require additional numerical dissipation to be stabilized: 2^{nd} and 4^{th} order artificial viscosity operators are used (see Lamarque [31]). The 2^{nd} order pseudo-Laplacian operator is triggered by a local sensor while the 4^{th} order hyperviscosity is applied everywhere in the domain (with some limitations). The estimation of the amount of the total artificial viscosity (not plotted here for brevity) shows that it is much lower than the physical (laminar + subgrid) viscosity everywhere in the region of interest except at some nodes close to the cylinder edges.

D. Averaging procedure

In order to extract statistical data from the instantaneous LES solutions, every three-dimensional field is averaged in the spanwise (z) direction which is statistically homogeneous. As a

first step, a 2D planar (constant-z) mesh matching the periodic boundaries of the domain is used to interpolate the 3D solution at 16 different z values. These 16 planar cuts are then summed to produce z-averaged 2D fields. Two different types of averages are then applied to these instantaneous fields following the experimental procedure by Lyn and Rodi [10]:

- A *time average*, noted $\overline{f}$ in the following, performed by averaging arithmetically any time-dependent flow variable $f(t)$. The corresponding fluctuation, noted f', is the root mean square value of f.

- A *phase average*, noted $\langle f \rangle$, obtained by averaging over every solution of constant ϕ, where ϕ is a given phase of the periodic vortex shedding. Following Lyn and Rodi [10], ϕ is defined from an instantaneous pressure signal $p(t)$ as plotted on Fig. 6.a. Sixteen probes have been regularly distributed in z at the center of the cylinder top wall to provide a mean pressure signal ("probe signal" on Fig. 6). This signal is then filtered by a low-pass second order Butterworth filter whose cutting frequency is equal to the shedding frequency measured by FFT as shown on Fig. 6.b. Minima and maxima of this filtered signal are used to define every half period of the vortex shedding which are then divided into 10 separate phase bins, leading to 20 bins for each full period. The reference phase $\phi = 0$ is taken at the half time between a maximum and a minimum of the pressure signal ($t^+ = t_n^+$ on Fig. 6.a). Every instantaneous z-averaged solution – about 40 solutions output per shedding period – is placed in its corresponding phase bin and an arithmetic averaging is performed for each phase. Phase-averaging f produces also a root mean square fluctuation noted $\langle f' \rangle$. $\langle f \rangle$ contains the contribution of the largest eddy scales associated with the periodic vortex shedding while $\langle f' \rangle$ is a residual fluctuation due to a smaller scale turbulence.

IV. Results and discussion

A. Validation of the flow dynamics

A first way to evaluate the accuracy of the present LES methods is to compare the results for global aerodynamic quantities with experiments and previous LES studies. Table 3 shows that both cases predicts a Strouhal number very close to the experimental value as well as most other LES. The

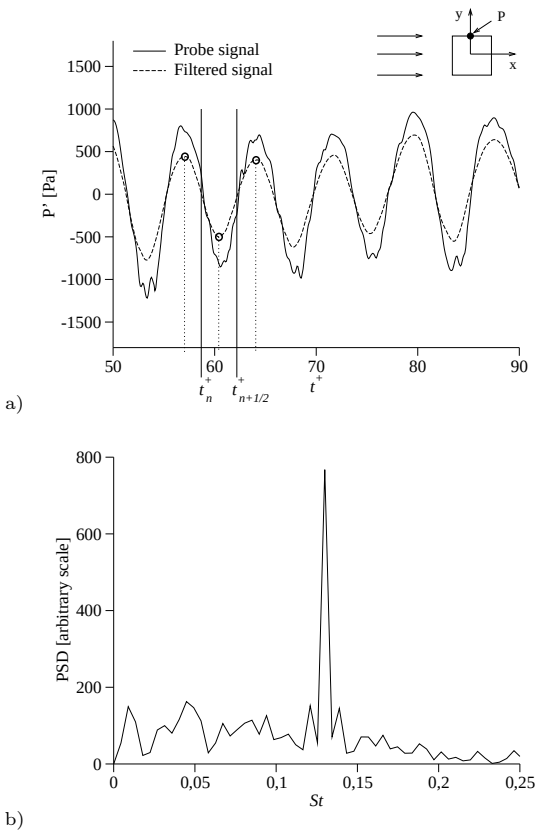

Fig. 6 Definition of the vortex shedding phase for case *LES-WF*: (a) sample of the unfiltered pressure fluctuation (after removing the mean value) and low-pass filtered pressure as a function of the non dimensional time $t^+ = t_{LES}/t_c$. (b) FFT of the unfiltered pressure signal.

drag coefficient predicted by case *LES-WF* is very close to the experiment while it is overpredicted for case *LES-WR* due to the underestimation of the pressure level on the rear side of the cylinder (discussed later). Concerning the length of the recirculation zone, both cases clearly underpredict the experimental values. According to Oudheusden *et al.* [26], this length may be quite sensitive to the freestream conditions. The level of turbulence as well as a non-zero incidence of the flow may modify the recirculation zone. Indeed, these authors show that an incidence of 5° leads to a 60% increase of the recirculation zone. In the present simulation, the freestream turbulence is zero while it is around 2% in the experiment by Lyn *et al.* [11].

Concerning the upstream velocity field at $x = -1$, Fig. 8 shows that the two present LES are in good agreement with the experimental results of Fohanno & Martinuzzi [23]: mean and rms profiles of streamwise and transverse velocity are very well recovered. The differences observed

Table 3 Global flow dynamics quantities and computational parameters of the two present LES cases (*LES-WF* and *LES-WR*) compared to the experimental results and other LES studies of the same flow configuration. St is the Strouhal number, C_D is the drag coefficient, l_r is the length of the recirculation zone, N_{cells} is the number of computational cells and y^+ is the mean Reynolds number of the wall computational cells.

	St	C_D	l_r	$N_{cells}\,(\times 10^6)$	y^+
Experiments					
Lyn *et al.* [11]	0.132 ± 0.004	2.1	1.38	–	–
Durao *et al.* [13]	0.133	–	1.33	–	–
Oudheusden *et al.* [26]	–	–	1.1	–	–
LES on structured grids					
Liou *et al.* [7]	0.133	2.14	0.91	0.37	–
Hangan & Kim [25]	0.134	2.065	1.29	0.107	–
Fureby *et al.* [6]	0.135	2.1	1.37	0.35	–
Barone *et al.* [8]	0.125	2.11	1.25	8.5	–
Rodi *et al.* [4] *(KAWAMU)*	0.15	2.58	1.25	0.195	–
LES on unstructured grids					
Camarri *et al.* [9] *(DM2)*	0.128	1.89	1.39	0.56	$10 - 100$
Present study *(LES-WF)*	0.132	2.21	0.71	3.2	24.5
Present study *(LES-WR)*	0.130	2.39	0.62	12.6	1.45

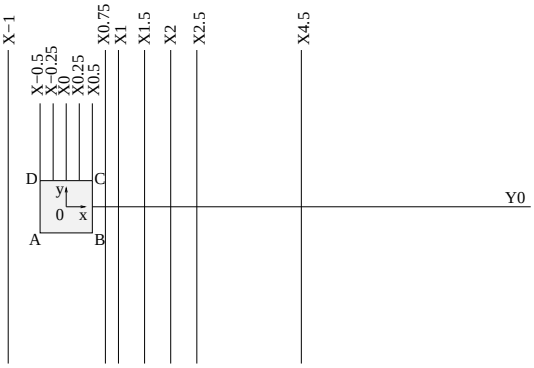

Fig. 7 Definition of the cutting lines used to show the profiles.

for the transverse velocity fluctuation are within the experimental error bars given by the authors

(which might have been overestimated, though). In this upstream region, the flow is irrotational and these velocity fluctuations are caused by the vortex shedding downstream the cylinder. This vortex shedding is evidenced on Fig. 9 thanks to an iso-surface of vorticity. One can see that the two-dimensional shear layer starting from the top leading edge of the cylinder becomes three-dimensional and generates the streamwise coherent structures, known as "ribs", that are observed experimentally [32, 33] and numerically [6]. These structures are very energetic and stay present in the near and intermediate wake of the cylinder, wrapping around the alternate spanwise rolls generated by the so-called von Kármán-Bénart instability.

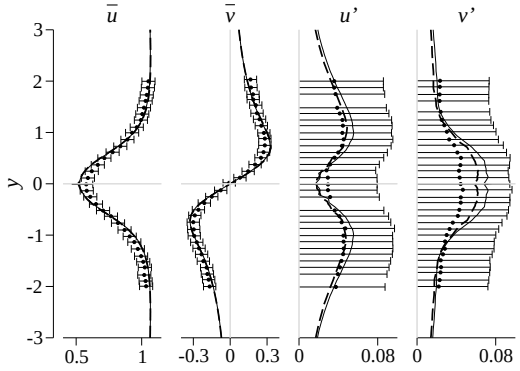

Fig. 8 Transverse profiles of time-averaged streamwise velocity, $\overline{u}$, transverse velocity, $\overline{v}$, streamwise velocity fluctuation, u', and transverse velocity fluctuation, v', upstream the cylinder at $x = -1$ (cut $X{-}1$ of Fig. 7): experimental results of Fohanno and Martinuzzi [23] (•) and present numerical results for cases *LES-WR* (——) and *LES-WF* (- - - -).

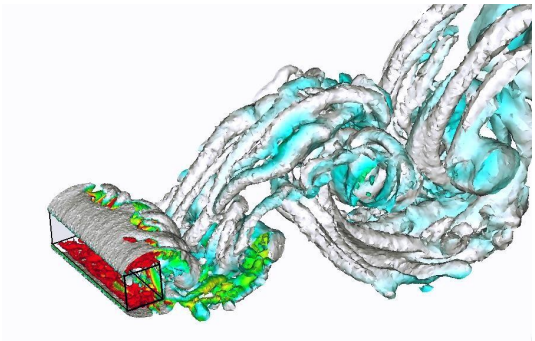

Fig. 9 Iso-surface of vorticity colored by temperature (case *LES-WF*).

The mean and fluctuating pressure fields around the cylinder are strongly influenced by the

vortex shedding phenomena and the transition from the irrotational to turbulent flow. Figure 10.a shows that the predicted pressure coefficient profiles agrees fairly well with the experimental data of Igarashi [24] and Bearman and Obasaju [12]. Discrepancies are observed for the *LES-WF* case of the side faces close to the leading edges. These unphysical values are due to the numerical errors induced by the poor spatial resolution of the separation region and the difficulty to deal with non-zero velocities on sharp edge nodes induced by the wall-function implementation method [1]. The pressure coefficient fluctuation C'_p traduces the variation of the pressure field caused by the vortex shedding and the turbulent motion. Figure 10.b shows that a qualitative agreement is obtained for C'_p in both LES cases. As for the average pressure coefficient, unphysical values of C'_p are obtained close to the edges with case *LES-WF*. On the side faces, the LES results are in better agreement with experimental data of Igarashi [24] than with those of Bearman and Obasaju [12]. In particular, case *LES-WR* captures very well the pressure fluctuation level on the upstream region of the side faces. However, it overestimates C'_p on the front and rear faces, probably due to some under-resolution of the boundary layer as shown by the y^+ profile of Fig. 5 on the front face and to the under-prediction of the rear face recirculation length zone (see below). Moreover, as mentioned by Bearman and Obasaju [12], the level of C'_p on the rear face is quite sensitive to the Reynolds number for $Re < 60\,000$.

As mentioned in the introduction, an accurate prediction of the wake flow behind a bluff-body is crucial for pratical configurations where the flow and heat transfer are strongly affected by various obstacles and their corresponding wakes. In the present wake region of the cylinder ($x > 3$), Fig. 11.a shows that the large streamwise and spanwise structures previously mentioned are responsible for a slow velocity recovery. While many LES studies tend to overpredict this recovery (see Rodi *et al.* [4]), both present cases are in a good agreement with the experimental results of Lyn *et al.* [11] and those of Fohanno & Martinuzzi [23]. Note that the recovery measured by Durao *et al.* [13] at lower Reynolds number is much faster. For ($x < 2$), both LES cases overpredict the axial velocity leading to a shorter recirculation length (as noticed before) and a lower backflow velocity, in comparison to the three experimental data. Figure 11.b shows that axial velocity fluctuations are accurately reproduced while transverse fluctuations tend to be overestimated by case *LES-WR* for $x < 1.5$ and

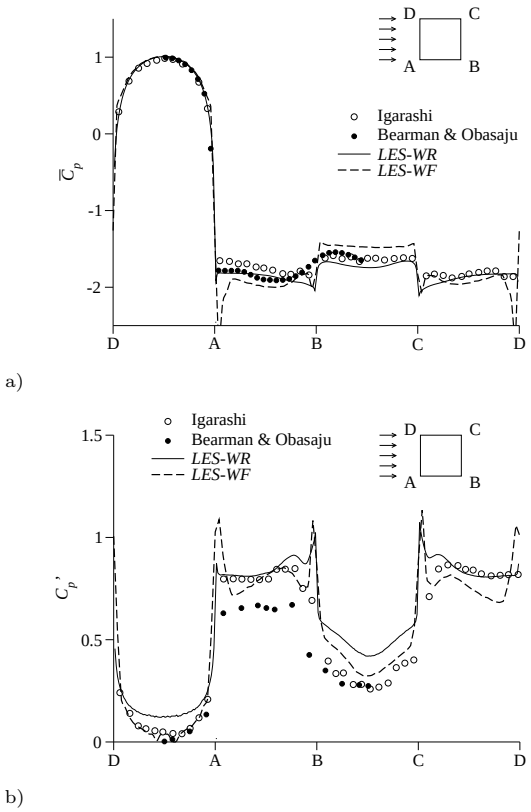

Fig. 10 Profiles of time-averaged pressure coefficient, C_p, (a) and fluctuation, C_p', (b) around the cylinder walls for the two LES cases compared to the experimental data of Igarashi [24] and Bearman and Obasaju [12].

$x > 5$. For the transverse profiles (Fig. 12 and 13), a very good agreement is generally obtained on mean and fluctuating velocity for both axial and transverse components in the two LES cases. Moreover, both present cases match closely the LES results of Hangan and Kim [25] (cut $X1.5$ of each figure). The error on the backflow prediction is visible on cuts $X1$ and $X1.5$ of Fig. 12.

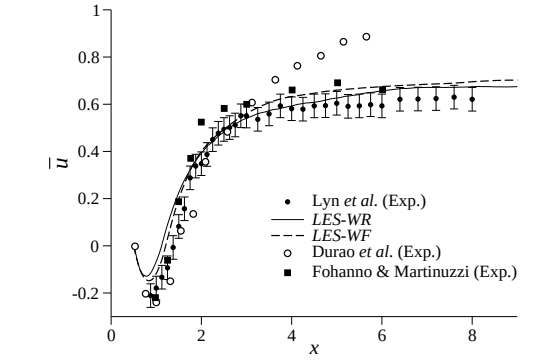

a)

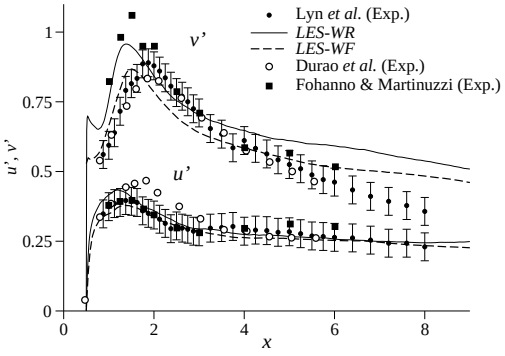

b)

Fig. 11 Longitudinal profiles of time-averaged streamwise velocity, $\overline{u}$, in the wake of the cylinder (cut $Y0$ of Fig. 7) (a). Corresponding streamwise, u', and transverse, v', velocity fluctuations (b). Experimental results of Lyn *et al.* [11] (•), Durao *et al.* [13] (○) and Fohanno and Martinuzzi [23] (■) and present numerical results for cases *LES-WR* (———) and *LES-WF* (– – – –).

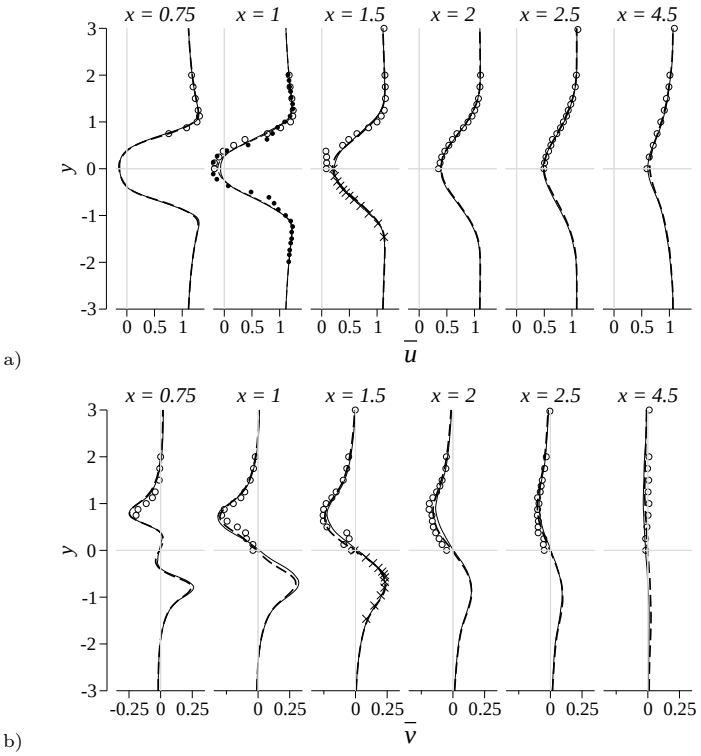

a)

b)

Fig. 12 Transverse profiles of time-averaged streamwise velocity, $\overline{u}$, (a) and transverse velocity, $\overline{v}$, (b) in the wake of the cylinder (cut $X0.75$ to $X4.5$ of Fig. 7): experimental results of Lyn *et al.* [11] ($\circ$), Fohanno and Martinuzzi [23] ($\bullet$), LES results of Hangan and Kim [25] ($\times$) and present numerical results for cases *LES-WR* (———) and *LES-WF* (– – – –).

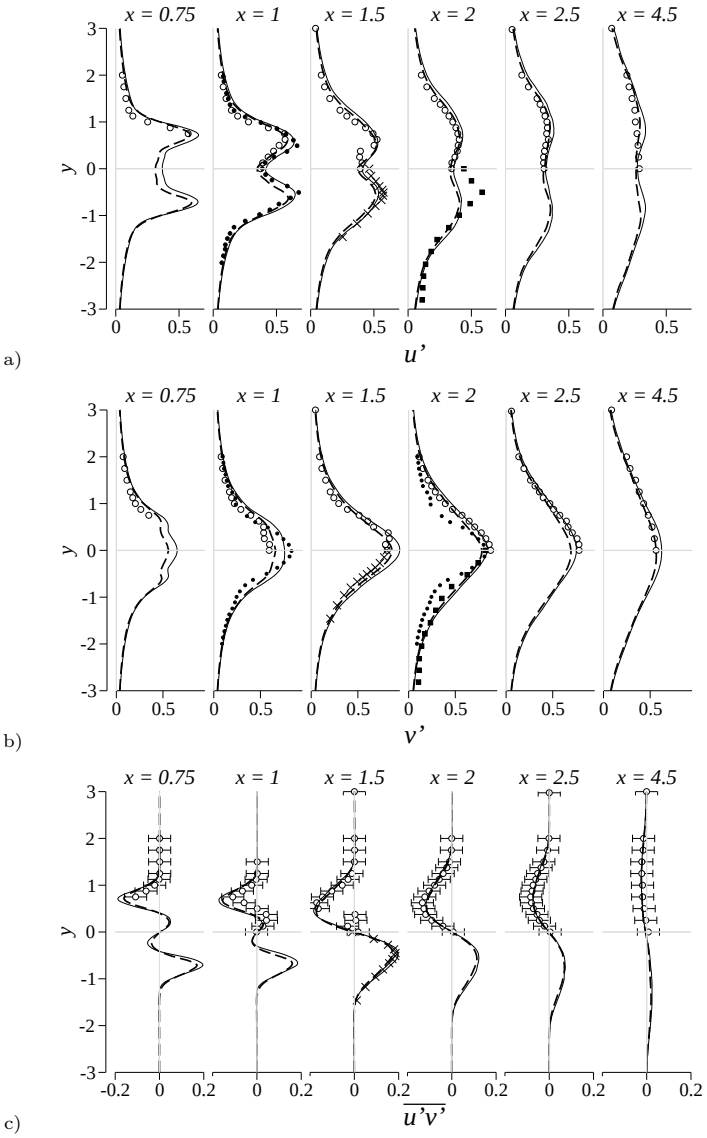

Fig. 13 Transverse profiles of time-averaged streamwise velocity fluctuation, u', (a), transverse velocity fluctuation, v', (b) and velocity correlation, $\overline{u'v'}$, (c) in the wake of the cylinder. Symbol legend: same as Fig. 12 and experimental results of Durao *et al.* [13] (■).

A way to evaluate how the LES captures the von Kármán-Bénart instability is to analyze the phase-averaged flow in the near wake of the cylinder. Figure 14 exhibits the axial profiles of transverse and axial phase-averaged velocity for three selected phases of the vortex shedding. Compared to other LES studies on structured grids, a better agreement is generally obtained with the transverse velocity for all phases and for both present LES cases. However, for $x > 5$, the phase velocity tends to be somewhat overestimated. Concerning the axial velocity, the maximum error occurs at phase $\phi = 162°$ for $x < 2$ where the backflow is strongly underestimated. Otherwise, both LES cases agree fairly well with the experiment. Phase-averaged turbulent fluctuations traduces the contribution of the eddy structures whose time scale is smaller than the vortex shedding period. In the present case, it includes the part from the streamwise "ribs" (see above in this section) as well as more uncorrelated fluctuations related to smaller scales. Most energy of these fluctuations is explicitly calculated in the LES. Figure 15 shows that a good agreement is obtained with the WALE subgrid model *(LES-WR)* for all phases while the Smagorinsky model *(LES-WF)* tends to underestimate the two first peaks. Figure 16 compares the phase-averaged transverse profiles of axial and transverse velocity at six axial positions of the near wake for two phases of the *LES-WR* case only (results are similar for the *LES-WF* case but not shown here for clarity). As expected, the velocity field varies strongly with phase due to the alternate vortex shedding. Except for cut $X1.5$ where little discrepancies are observed, the LES captures accurately these variations by matching closely the experimental data.

The flow dynamics near the side faces of the cylinder is also of interest because both the flow field and the heat transfer around the cylinder are strongly influenced by this region where separation and recirculation occur. Figure 17.a compares the mean streamwise velocity profiles given by the two present LES with the experimental results of Lyn and Rodi [10] and the LES results of Hangan and Kim [25]. In both cases, the averaged position and thickness of the shear layer induced by the flow separation are well reproduced. For $0 \leq x \leq 0.5$, the velocity intensity in the backflow region is underpredicted by case *LES-WR* while it is quite well captured by case *LES-WF* and Hangan and Kim. Streamwise velocity fluctuations given by Fig. 17.b traduce the flapping of the shear layer as well as the turbulence activity in the backflow zone. Results from case *LES-WF*, which are

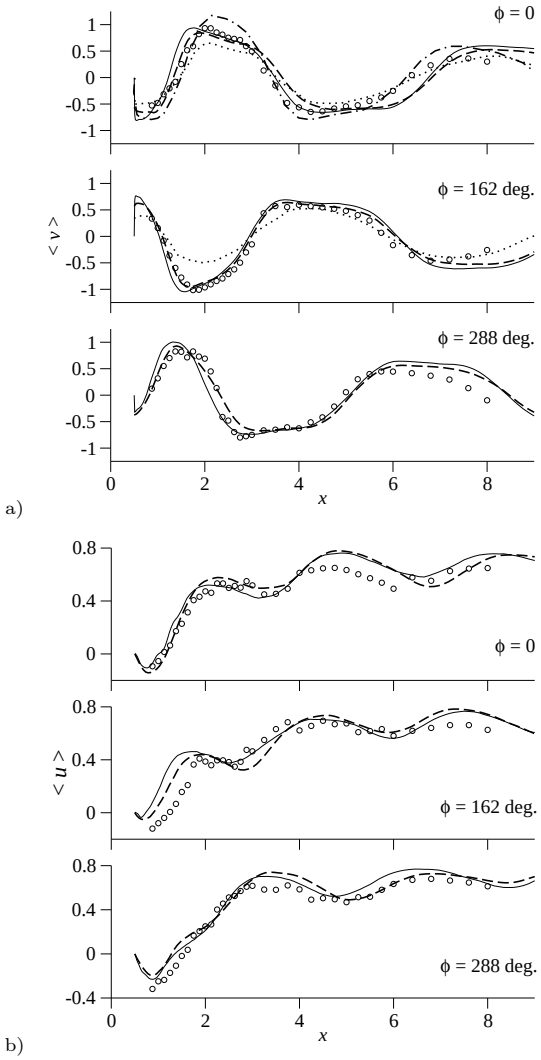

Fig. 14 Longitudinal profiles of phase-averaged transverse velocity, $\langle v \rangle$, (a) and streamwise velocity, $\langle u \rangle$, (b) in the wake of the cylinder at three selected phase angles: experimental results of Lyn *et al.* [11] (○), LES results of Liou *et al.* [7] (·····), case KAWAMU in Rodi *et al.* [4] (— · —) and present results for cases *LES-WR* (———) and *LES-WF* (– – – –).

very close to those of Hangan and Kim, agree quite well with the experimental data although they overpredict u' in the backflow. On the other side, case *LES-WR* tends to overpredict u' in the shear layer but gives better results in the backflow zone. One can argue that this overestimation of u' by both approaches would be worse if the subgrid scale contribution were added to the plotted resolved fluctuation. However, the subgrid energy contribution is negligible compared to the resolved energy in this region where the grid resolution is rather high.

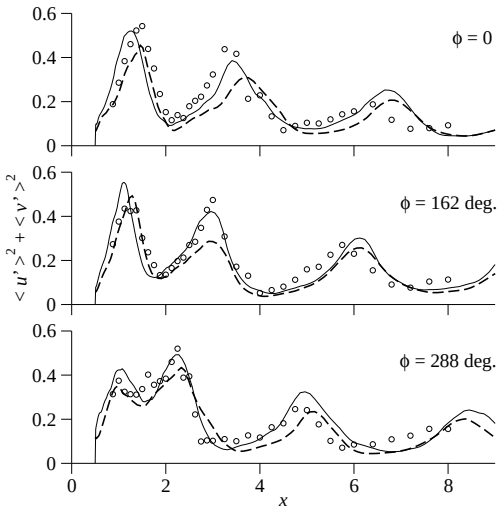

Fig. 15 Longitudinal profiles of phase-averaged turbulent fluctuation, $\langle u'^2 + v'^2 \rangle$, in the wake of the cylinder. See Fig. 14 for symbols legend.

The phase evolution of the backflow is detailed on Fig. 18 by plotting the phase-averaged streamwise velocity and its fluctuation at six selected vertical locations above the top side wall. Both LES approaches give similar results and are quite close from the experimental data. However, the downward motion of the shear layer is in advance in the simulations compared to the experiment (see plots at $y = 0.675$, 0.75 and 0.8455) while the upward motion is accurately synchronized. Similar errors are observed on the fluctuating component $\langle u' \rangle$. Moreover, the excessive values of $\langle u' \rangle$ observed in the LES at some phases of the vortex shedding are consistent with the overestimation of the time-averaged fluctuation previously observed on u' profiles (see Fig. 17.b).

B. Validation of the heat transfer

Now that both wall-treatment approaches have proved to be accurate for the flow dynamics, their capacity to predict convective heat transfer is evaluated by comparing the computed Nusselt number with experimental data. Table 4 shows that the wall-function strongly underpredicts the global Nusselt $\overline{Nu}_g$ — obtained by space-averaging the local Nusselt profiles around the square contour — whereas the wall-resolved approach presents a very good accuracy.

A more detailed comparison is provided by the profiles of the time-averaged Nusselt number

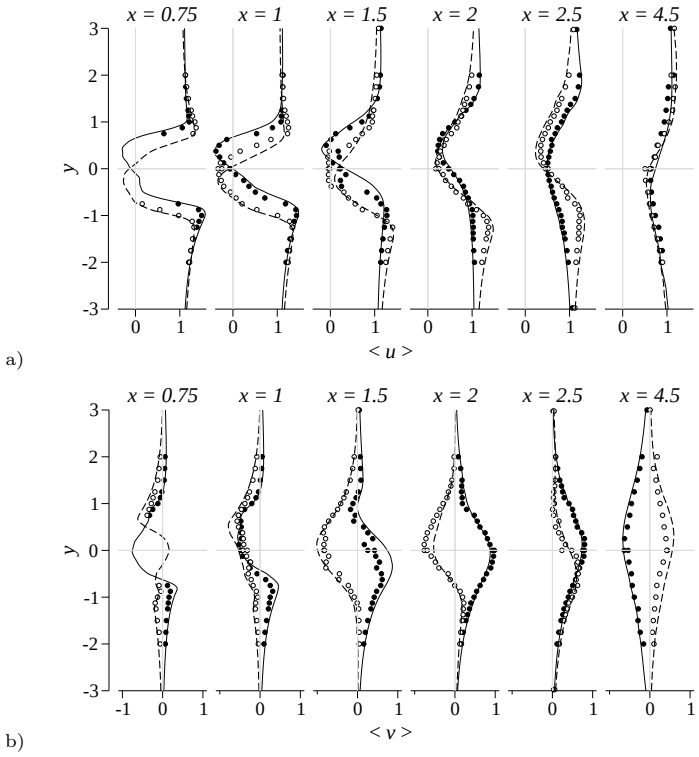

Fig. 16 Transverse profiles of phase-averaged streamwise velocity, $\langle u \rangle$, (a) and transverse velocity, $\langle v \rangle$, (b) in the wake of the cylinder at two selected phase angles: experimental results of Lyn *et al.* [11] at $\phi = 0°$ ($\circ$) and $108°$ ($\bullet$) and present results for case *LES-WR* at $\phi = 0°$ (———) and $108°$ (- - - -).

Table 4 Global Nusselt number $\overline{Nu}_g$ of the two present LES compared to the experimental correlation of Igarashi [14] (Eq. (14)) for the given Reynolds number $Re = 22\,050$.

	$\overline{Nu}_g$	Error
Igarashi [14]	103.0	–
LES-WF	46.1	−55%
LES-WR	101.6	−1.36%

$\overline{Nu}$ around the cylinder walls. Figure 19 shows that all experimental profiles have similar shapes and levels although the profiles from Yoo *et al.* [15] present a slightly larger amplitude than those of Igarashi [14], justifying the scaling of Eq. (15). As expected from the global Nusselt results (Table 4), the wall-function approach does not predict the right level at any position of the cylinder face. Even

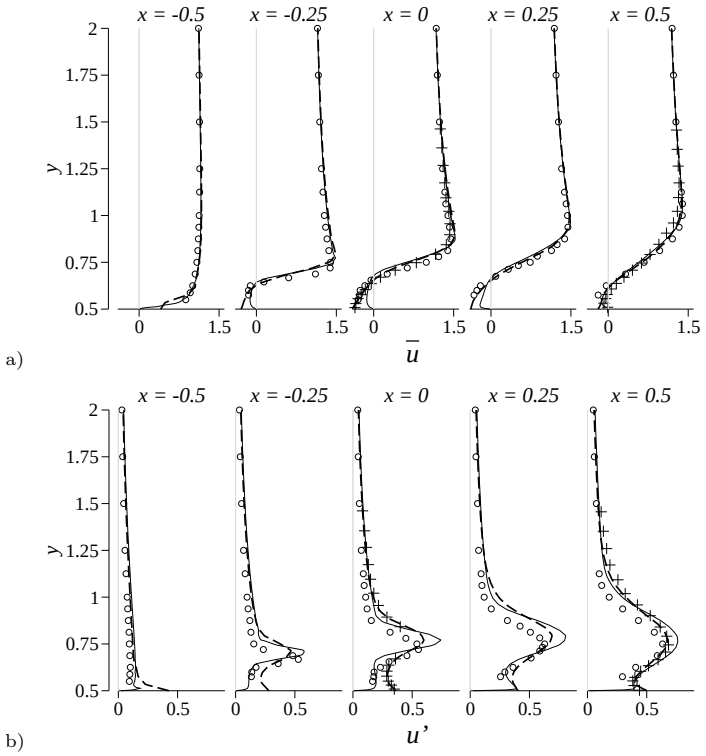

Fig. 17 Transverse profiles of time-averaged streamwise velocity, $\overline{u}$, (a) and fluctuation, u', (b) on the top face of the cylinder (cuts X–0.5 to X0.5 of Fig. 7): experimental results of Lyn and Rodi [10] ($\circ$), LES results of Hangan and Kim [25] ($+$) and present LES results for cases *LES-WR* (——) and *LES-WF* (- - - -).

the shape of the profiles is not properly retrieved. Actually, this bluff-body flow does not verify the wall-function assumption anywhere around the cylinder: the impinging flow with a stagnation point on the front face, the flow separation on the side faces and the backflow on the back face that occur here are not compatible with the constant pressure gradient and steady attached flow assumption of the wall-function model. Piomelli [34] showed that wall-function cannot predict accurately the near-wall dynamics and wall stresses of detached flows and oscillating flows. Nevertheless, for the flow dynamics only, the results of section IV A have shown that good predictions are obtained in the *LES-WF* case although the flow breaks the model requirements. In reality, the velocity field around the cylinder results in flow separation and vortex shedding phenomena that depend slightly on the wall friction. As a consequence, the wall pressure and the resulting drag force are quite well predicted (see Fig. 10 and Table 3) because they depend mainly on large eddy motions that are not

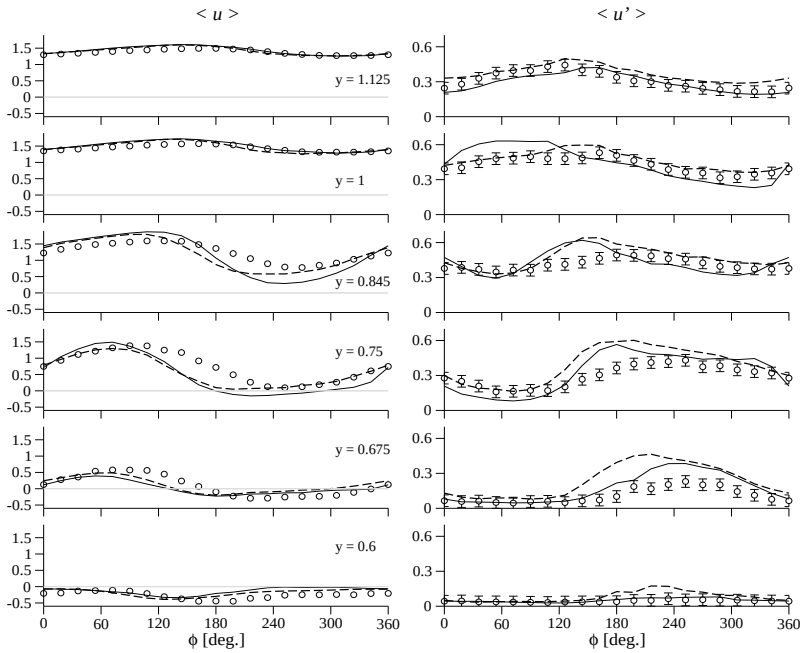

Fig. 18 Evolution of phase-averaged streamwise velocity, $\langle u \rangle$, and fluctuation, $\langle u' \rangle$, as a function of the phase at six selected vertical positions above the top side of the cylinder ($x = 0.25$): experimental results of Lyn and Rodi [10] ($\circ$) and LES results for cases *LES-WR* (——) and *LES-WF* (– – – –).

very sensitive to the viscous near-wall effects. The wall heat flux, however, is directly computed by the wall-function model that fails to mimic the turbulent heat transfer in the wall boundary layer when the model assumptions are not verified. Moreover, the Reynolds analogy used in the thermal wall-function model may not be fully valid for the range of y^+ values $(20 - 50)$ obtained in this calculation.

Contrary to the wall-function approach, the wall-resolved approach is able to reproduce the experimental data, particularly on the front and rear faces (where the agreement is better with the data of Yoo *et al.*). On the side faces, the Nusselt number is slightly underestimated. This error can be related to the underprediction of the backflow mean velocity mentioned in section IV A, which may lead to a lower convective flux close to the cylinder walls. One can notice that the Nusselt error is not correlated to the high value of y^+ mentioned in section III C and visible on Fig. 5, meaning that, though y^+ is larger than 2 in some part of the cylinder wall, the space resolution of

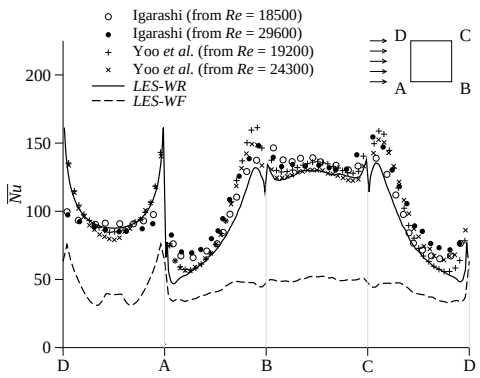

Fig. 19 Profiles of time-averaged local Nusselt number, $\overline{Nu}$, around the cylinder walls : experimental results of Igarashi [14] ($\circ$ **and** $\bullet$) **and of Yoo *et al.* [15]** ($+$ **and** $\times$) **scaled using Eq. (15) and compared to the present LES results** (——— **and** – – – –).

the near-wall region is adequate to predict the wall heat flux. Now that the wall-resolved approach is validated for the prediction of heat transfer, an unsteady analysis of the *LES-WR* simulation is performed in the next section to investigate the heat transfer mechanism in the single cylinder configuration.

C. Analysis of the unsteady heat transfer (case *LES-WR*)

By superimposing phase-averaged Nusselt profiles, stream lines and temperature field, Fig. 20 highlights how the heat flux from the cylinder wall is coupled to the periodic vortex shedding. Each face of the cylinder is now commented for four chosen phases $\phi = 0°, 36°, 72°, 126°$ that illustrate conveniently the first half-period of vortex shedding (the $\phi + 180°$ values are not treated since they correspond to the second half-period where the flow is symmetric).

Front face: The incoming flow is laminar and presents a stagnation point that oscillates slightly up and down with the phase. As a consequence, the Nusselt profile is almost steady, with a minimum around the stagnation point and maxima close to the leading edges due to the flow acceleration. Though the flow regime is laminar, the near-wall region is continuously blown by the incoming cold fluid whatever the phase so that the heat flux close to the edges is higher on the front face than on the side faces where hot fluid recirculation occurs (see below).

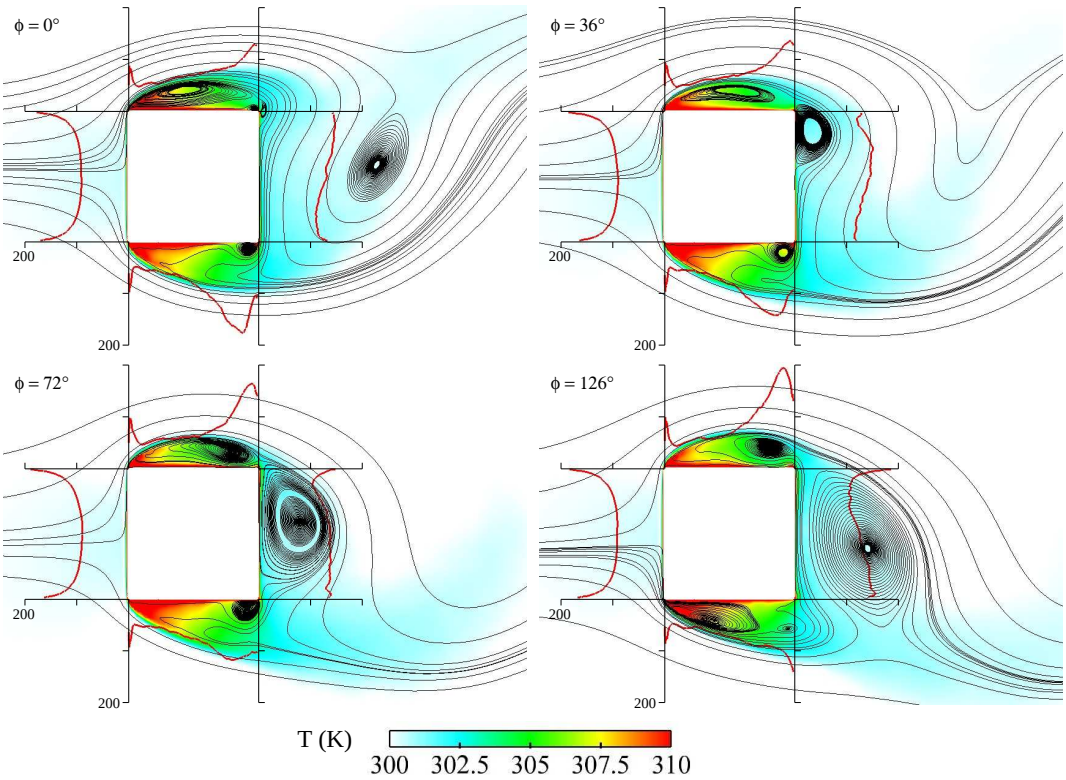

Fig. 20 Phase-averaged quantities taken at four selected phase angles of case *LES-WR*: Nusselt number profiles at each side of the cylinder (scales are all identical), velocity stream lines and flow temperature distribution.

Rear face: Here, no hot fluid can accumulate because the von Kármán-Bénart instability provokes a "sweep" of the wall by a periodically upward and downward flow whose oscillations are highlighted by the friction coefficient curve of Fig. 21.a. This oscillating flow features a transient reattachment of the shear layer on the rear face (see phases $\phi = 0° - 72°$) as observed experimentally by Igarashi [24]. This guaranties that cold fluid from outside the shear layer is carried towards the wall at any phase, that is why the mean rear face Nusselt number is higher than the one of the front face and varies little with phase (see Fig. 21.b). Moreover, the flow is fully turbulent in this region (see Fig. 9) so the wall heat transfer is also enhanced by the small turbulent eddies (whose time scale is smaller than the shedding period).

Top and bottom faces: In the leading edge region, mean and fluctuating velocities are quite low (see Fig. 17 of section IV A) and hot fluid is trapped by recirculation, leading to a low Nusselt

number at all phases: the temperature field around the cylinder (Fig. 20) shows clearly the correlation between hot fluid close to the near-wall region and a low wall heat flux. At $\phi = 0°$ the center of the recirculation region is located upstream and convective effects are rather low close to the trailing edge. As described in Lyn and Rodi [10], this eddy moves to a downstream position and stays there from phase $\phi = 72°$ to $126°$ approximatively (and the corresponding phases $\phi = 252°$ to $306°$ for the bottom face). Once located near the trailing edge, it increases the wall heat flux from the adjacent wall by thinning the boundary layer and carrying some cold fluid from outside the shear-layer. This is confirmed more quantitatively by Fig. 21 which shows that the increase in the mean Nusselt number of the top and bottom faces (Fig. 21.b) just follows the increase in the mean friction coefficient, $\langle C_f \rangle$, due to the downstream eddy structure (Fig. 21.a, respective curves). The time delay between the maximum wall friction — i.e. the maximum convective effect — and the maximum of heat flux is probably due to the time needed by the eddy vortex to bring some fresh fluid close to the wall. One can notice also that the rear face flow reattachment induces another flow separation on the bottom trailing edge and a corresponding vortex attached to the bottom face for phases $\phi = 0° - 72°$ (or the corresponding $\phi = 180° - 252°$ for the top face). Compared to the eddy structure induced by the upstream flow separation, this vortex rotates in the opposite direction and provides the side face region with cold fluid coming from the rear region as shown by the streamlines. This vortex is also responsible for a local Nusselt peak which vanishes gradually as the rear face flow reattachment is cancelled by the main vortex shedding (see $\phi = 126°$). As a consequence, the mean Nusselt number of the bottom face decreases from $\phi = 0°$ to $180°$ as shown by Fig. 21.b.

Finally, because the Nusselt variations of the top and bottom faces are out of phase and the Nusselt of the front and rear faces vary little, the global Nusselt number presents a very low variation with phase (Fig. 21.b).

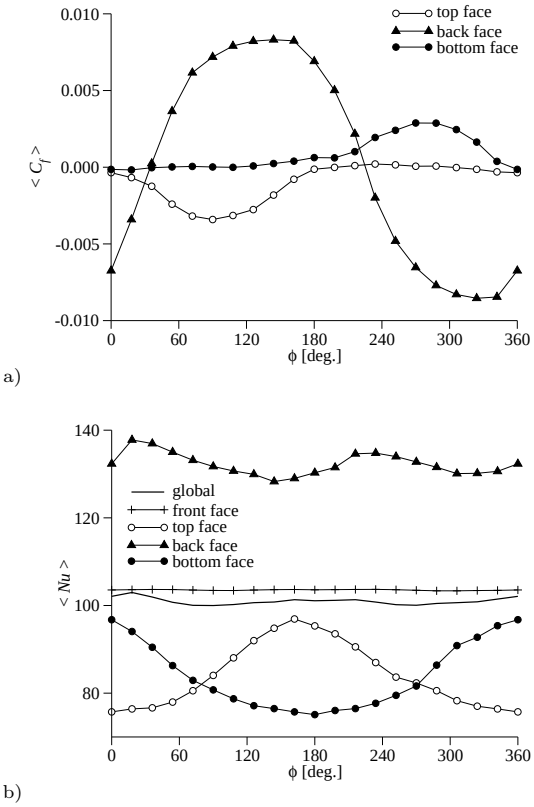

Fig. 21 Space-averaged value of the phase-averaged algebraic friction coefficient, $\langle C_f \rangle$, (a) and Nusselt number, $\langle Nu \rangle$, (b) on different faces of the cylinder as a function of the phase ϕ.

Conclusion

The flow around a square cylinder is a relevant model for testing a computational method for turbulent heat transfer because it features the main characteristics of typical industrial flows in complex geometry: flow separation and recirculation, vortex shedding and wake flow. In this configuration, two approaches of heat transfer prediction by large eddy simulation using unstructured grids have been compared: 1) a method using a full tetrahedra grid along with an algebraic wall-function model and a standard Smagorinsky subgrid scale model and 2) a method using a hybrid tetrahedra/prisms grid along with the WALE subgrid scale model in order to solve explicitely the wall boundary layer.

Compared to a full tetrahedra approach, the major advantage of using prisms layers to solve the boundary layer is to reduce the computational cost of the simulation. By increasing the number of computational cores up the code acceleration limit, the ratio of 40 in CPU time between approach

2) and 1) may be finally reduced down to a ratio of 5 in terms of execution time. However, the benefit of using prisms layers depends strongly on the ability of the numerical method to handle stretched prismatic cells.

In terms of flow dynamics, despite some underestimation of the size and intensity of the recirculation zone behind the cylinder, both approaches have successfully reproduced the experimental results [10, 11] as well as other LES data. In particular, the near-wake predictions have been carefully validated by comparing the time- and phase-averaged statistics of the vortex shedding flow. This is a promising result for simulating real cases where the complex geometry induces multiple turbulent wakes that have a major influence on the flow and heat transfer. Satisfactory results have also been obtained for the velocity field near the side faces of the cylinder, excepting some local errors observed with method 1) very close to the sharp edges. In general, the flow dynamics predictions have shown a rather low sensitivity to wall-treatment and the subgrid model. Considering that method 1) is 40 times less expensive in terms of computational time, it seems adequate if only the flow dynamics is of interest. However, as far as heat transfer is concerned, this algebraic method fails to predict the local and global Nusselt numbers because the present flow does not verify the wall-function model assumption of steady attached flow at high wall Reynolds values. The accuracy of the thermal wall-function model for higher wall Reynolds was not investigated here because such configurations would not be representative of the typical aeronautical applications targeted in the present study (see section I). On the contrary, the second method is capable to reproduce with a good accuracy the experimental data for the Nusselt distribution around the cylinder [14, 15]. The phase-averaged analysis reveals the unsteady mechanism responsible for this distribution. On the side faces, the heat flux stays low close the leading edges because of low velocities and hot fluid recirculation. Close to the trailing edges, however, the heat flux strongly varies with phase and it is maximum when the vortex shedding produces an eddy structure adjacent to the wall. On the rear face, the Nusselt number is quite high whatever the phase because of the periodic flow featuring alternatively reattachment and large eddy vortices.

Acknowledgements

Fahmi Ben Ahmed is gratefully acknowledged for its contribution to the present work. We also want to thank Olivier Cabrit for the helpful discussions.

References

[1] Schmitt, P., Poinsot, T., Schuermans, B., and Geigle, K., "Large-eddy simulation and experimental study of heat transfer, nitric oxide emissions and combustion instability in a swirled turbulent high pressure burner," *Journal of Fluid Mechanics*, Vol. 570, 2007, pp. 17–46.

[2] Bosch, G. and Rodi, W., "Simulation of vortex shedding past a square cylinder near a wall," *International Journal of Heat and Fluid Flow*, Vol. 17, No. 3, 1996, pp. 267–275.

[3] Bosch, G. and Rodi, W., "Simulation of vortex shedding past a square cylinder with different turbulence models," *International Journal for Numerical Methods in Fluids*, Vol. 28, No. 4, 1998, pp. 601–616.

[4] Rodi, W., Ferziger, J., Breuer, M., and Pourquiée, M., "Status of Large Eddy Simulation: Results of a Workshop," *Journal of Fluids Engineering*, Vol. 119, 1997, pp. 248–262.

[5] Kim, S. and Boysan, F., "Application of CFD to environmental flows," *Journal of Wind Engineering & Industrial Aerodynamics*, Vol. 81, No. 1-3, 1999, pp. 145–158.

[6] Fureby, C., Tabor, G., Weller, H., and Gosman, A., "Large eddy simulations of the flow around a square prism," *AIAA Journal*, Vol. 38, No. 3, 2000, pp. 442–452.

[7] Liou, T.-M., Chen, S.-H., and Hwang, P.-W., "Large Eddy Simulation of Turbulent Wake Behind a Square Cylinder With a Nearby Wall," *Journal of Fluids Engineering*, Vol. 124, No. 1, 2002, pp. 81–90.

[8] Barone, M. and Roy, C., "Evaluation of Detached Eddy Simulation for Turbulent Wake Applications," *AIAA Journal*, Vol. 44, No. 12, 2006, pp. 3062–3071.

[9] Camarri, S., Salvetti, M., Koobus, B., and Dervieux, A., "Large-eddy simulation of a bluff-body flow on unstructured grids," *International Journal for Numerical Methods in Fluids*, Vol. 40, No. 11, 2002.

[10] Lyn, D. A. and Rodi, W., "The flapping shear layer formed by flow separation from the forward corner of a square cylinder," *Journal of Fluid Mechanics*, Vol. 267, 1994, pp. 353–376.

[11] Lyn, D. A., Einav, S., Rodi, W., and Park, J., "A laser-Doppler velocimetry study of ensemble-averaged characteristics of the turbulent near wake of a square cylinder," *Journal of Fluid Mechanics*, Vol. 304, 1995, pp. 285–319.

[12] Bearman, P. and Obasaju, E., "An experimental study of pressure fluctuations on fixed and oscillating square-section cylinders," *Journal of Fluid Mechanics*, Vol. 119, 1982, pp. 297–321.

[13] Durão, D., Heitor, M., and Pereira, J., "Measurements of turbulent and periodic flows around a square cross-section cylinder," *Experiments in Fluids*, Vol. 6, No. 5, 1988, pp. 298–304.

[14] Igarashi, T., "Heat transfer from a square prism to an air stream," *International journal of heat and mass transfer*, Vol. 28, No. 1, 1985, pp. 175–181.

[15] Yoo, S., Park, J., Chung, C., and Chung, M., "An Experimental Study on Heat/Mass Transfer From a Rectangular Cylinder," *Journal of Heat Transfer*, Vol. 125, 2003, pp. 1163.

[16] Moureau, V., Lartigue, G., Sommerer, Y., Angelberger, C., Colin, O., and Poinsot, T., "High-order methods for DNS and LES of compressible multi-component reacting flows on fixed and moving grids," *Journal of Computational Physics*, Vol. 202, No. 2, 2005, pp. 710–736.

[17] Schönfeld, T. and Rudgyard, M., "A cell-vertex approach to local mesh refinement for the 3-D Euler equations," *32nd AIAA Aerospace Sciences Meeting & Exhibit*, AIAA, Reno, NV, USA, 1994, p. 318.

[18] Colin, O. and Rudgyard, M., "Development of high-order Taylor-Galerkin schemes for unsteady calculations," *Journal of Computational Physics*, Vol. 162, No. 2, 2000, pp. 338–371.

[19] Nicoud, F. and Ducros, F., "Subgrid-Scale Stress Modelling Based on the Square of the Velocity Gradient Tensor," *Flow, Turbulence and Combustion*, Vol. 62, No. 3, 1999, pp. 183–200.

[20] Poinsot, T. and Lele, S., "Boundary conditions for direct simulations of compressible viscous flows," *Journal of Computational Physics*, Vol. 101, No. 1, 1992, pp. 104–129.

[21] Wolf, P., Balakrishnan, R., Staffelbach, G., Gicquel, L., and Poinsot, T., "Using LES to Study Reacting Flows and Instabilities in Annular Combustion Chambers," *Flow, Turbulence and Combustion*, Vol. 88, 2012, pp. 191–206, 10.1007/s10494-011-9367-7.

[22] Piomelli, U. and Balaras, E., "Wall-layer models for large-eddy simulations," *Annual Review of Fluid Mechanics*, Vol. 34, No. 34, 2002, pp. 349–374.

[23] Fohanno, S. and Martinuzzi, R. J., "A Phase-Averaged Analysis of Droplet Dispersion in the Wake of a Square Cylinder in a Uniform Stream," *Journal of Fluids Engineering*, Vol. 126, No. 1, 2004, pp. 110–119.

[24] Igarashi, T., "Characteristics of the Flow around a Square Prism," *Bulletin of JSME*, Vol. 27, No. 231, 1984, pp. 1858–1865.

[25] Hangan, H. and Kim, J., "Aerodynamic slot-control for 2D square prisms," *Journal of Wind Engineering & Industrial Aerodynamics*, Vol. 91, No. 12-15, 2003, pp. 1847–1857.

[26] Oudheusden, B., Scarano, F., Hinsberg, N., and Watt, D., "Phase-resolved characterization of vortex shedding in the near wake of a square-section cylinder at incidence," *Experiments in Fluids*, Vol. 39, No. 1, 2005, pp. 86–98.

[27] Sparrow, E., Abraham, J., and Tong, J., "Archival correlations for average heat transfer coefficients for non-circular and circular cylinders and for spheres in cross-flow," *International Journal of Heat and Mass Transfer*, Vol. 47, No. 24, 2004, pp. 5285–5296.

[28] Cho, K., Irvine, T., and Karni, J., "Measurement of the diffusion coefficient of naphthalene into air," *International Journal of Heat and Mass Transfer*, Vol. 35, No. 4, 1992, pp. 957–966.

[29] Kallinderis, Y. and Ward, S., "Prismatic grid generation for three-dimensional complex geometries," *AIAA Journal*, Vol. 31, No. 10, 1993, pp. 1850–1856.

[30] Kallinderis, Y., Khawaja, A., and McMorris, H., "Hybrid prismatic/tetrahedral grid generation for viscous flows around complex geometries," *AIAA Journal*, Vol. 34, No. 2, 1996, pp. 291–298.

[31] Lamarque, N., *Schémas numériques et conditions limites pour la simulation aux grandes échelles de la combustion diphasique dans les foyers d' hélicoptère*, Ph.D. thesis, Institut National Polytechnique de Toulouse, France, 2007.

[32] Hussain, A. and Hayakawa, M., "Eduction of large-scale organized structures in a turbulent plane wake," *Journal of Fluid Mechanics*, Vol. 180, 1987, pp. 193–229.

[33] Dobre, A. and Hangan, H., "Investigation of the three-dimensional intermediate wake topology for a square cylinder at high Reynolds number," *Experiments in Fluids*, Vol. 37, No. 4, 2004, pp. 518–530.

[34] Piomelli, U., "Wall-layer models for large-eddy simulations," *Progress in Aerospace Science*, Vol. 44, No. 6, 2008, pp. 437–446.